Application of semi-automated methods for extraction of geological surface orientations: A case study from the outer Garhwal Himalaya

Bhagirathi Panigrahi[1,*] , D C Srivastava[1], Sonal Tiwari[2],
Amar Agarwal[2], Bitihotri Rit[1] and Syed Shahid Akhtar[1]

[1]*Department of Earth Sciences, Indian Institute of Technology, Roorkee 247 667, India.*
[2]*Department of Earth Sciences, Indian Institute of Technology, Kanpur 201 816, India.*
*Corresponding author. e-mail: b_panigrahi@es.iitr.ac.in

The application of Unmanned Aerial Vehicles (UAV) is becoming increasingly common in geological mapping. The acquired UAV images help in building a 3D virtual outcrop model after processing. In particular, the use of UAV provides a rapid and low-cost method for estimating planar discontinuity orientation in inaccessible outcrops. Several open-access software packages are now available for automatic extraction of the orientation of planar structures using point cloud data generated from UAV images. This study demonstrates software applications for extracting geological discontinuities and compares the results with direct field observations in the outer part of the Garhwal Lesser Himalaya. Two types of geological surfaces, namely, the bedding surface and the fracture surface, are tested by processing point clouds in the discontinuity set extractor (DSE) and the FACETS (cloudcompare) software. Both the DSE and the FACETS require the availability of distinct 3-D exposures and clean point clouds on virtual Outcrop models. Results from both the software deviate from the field observations by a few degrees. Between the two software, FACETS gives relatively more accurate results than the DSE. The compass tool is an additional advantage in the cloudcompare (FACETS). These techniques have been successfully demonstrated in rock mass characterization and slope stability studies. In general, the semi-automatic methods are useful in studies requiring the orientation of a well-exposed single surface or several surfaces in a small area that is inaccessible. These techniques, however, become time-intensive due to noisy data in geologically complex areas where the rocks are cut by multiple sets of discontinuities.

Keywords. UAV images; FACETS; DSE; semi-automatic; geological discontinuities.

1. Introduction

Field observation on surface orientation is time-and-cost intensive and limited by factors such as the accessibility of the outcrops, the ruggedness of the terrains, and the pandemic-hit periods, such as the global pandemic – COVID-19. As a potential alternative, remote sensing image acquisition techniques, such as Laser imaging Detection And Ranging (LiDAR), Terrestrial structure from motion (Tsfm), and Aerial structure from motion (Asfm) by Unmanned Aerial Vehicle (UAV) could

be used for extraction of 3-D data from outcrops (Passchier and Exner 2010; Westoby *et al.* 2012; Riquelme *et al.* 2014; Dewez *et al.* 2016; Wang *et al.* 2019; Giordan *et al.* 2020; Herrero *et al.* 2022; Ghosh *et al.* 2023). These semi-automatic methods have been extensively tested for fracture orientation in rock mass characterization studies (Lapponi *et al.* 2011; Vöge *et al.* 2013; Vasuki *et al.* 2014; Assali *et al.* 2016; Casini *et al.* 2016; Chen *et al.* 2016, 2017; Dewez *et al.* 2016; Viana *et al.* 2016; Cao *et al.* 2017; Guo *et al.* 2017; Wang *et al.* 2017; Akara *et al.* 2020; Kong *et al.* 2021; Wu *et al.* 2021; Daghigh *et al.* 2022; Herrero *et al.* 2022). In a comparative study, Cawood *et al.* (2017) demonstrate that the UAV models provide more accurate results than those of the LiDAR or the Tsfm models.

Several recent software packages, such as DSE (Discontinuity Set Extractor, Riquelme *et al.* 2014), FACETS in cloudcompare (Dewez *et al.* 2016), and RANSAC (Vasuki *et al.* 2014), are available for semi-automatic extraction of orientations of geological surfaces from the UAV models (Bieniawski 1989; Hudson 2001; Riquelme *et al.* 2014; Dewez *et al.* 2016; Wang *et al.* 2019). The success of these methods has been tested mostly on a single fracture, slope, or in a relatively small area of a few hundred square meters (Riquelme *et al.* 2014; Dewez *et al.* 2016; Herrero *et al.* 2022). Here, we use UAV images for demonstration of the DSE and the FACETS software in an 840 m^2 area of folded and fractured rocks in the Himalayan terrain and compare the results with the direct field observations.

2. Geological setting of the study area

The basic framework of geology of the Garhwal–Kumaun Lesser Himalaya was laid down by Auden (1934), Bhargava (1972), Valdiya (1980), Ravi Shanker Kumar *et al.* (1993) and Kumar (2005). The Main Boundary Thrust, an orogen-scale lineament, is the most conspicuous tectonic structure in the outer parts of the Himalaya. The thrust dips to the north and emplaces the Lesser Himalaya over the Sub-Himalaya. Several isolated Krol-synclines, each comprising the Proterozoic sedimentary rocks predominantly, occur on the hanging wall of the Main Boundary Thrust (figure 1).

The study area lies on the southwestern limb of the Garhwal syncline, one of the several

Krol-synclines (figure 1). The syncline contains the Baliana Group, the Krol Group, and the Tal Group rocks in younging order. The Baliana Group consists of Blaini diamictite, thin bands of sandstone and shale, cap dolomite, and the shale/phyllite of the Infra-Krol Formation. The overlying Krol Group consists of three formations; Mahi Formation or Lower Krol (Krol-A), Jarashi Formation or Middle Krol (Krol-B), and Kaudiyala Formation or Upper Krol (Krol-C, D and E). The core of Garhwal syncline is occupied by the Tal Group, which is overlain by shell limestone and Subathu Formation.

Situated on the southwestern bank of the Ganges River near Tapovan, N 30°08.038′, E 78°19.979′, the study area exposes a carbonate sequence that belongs to the Krol-A or Mahi Formation (figure 2). The rock types vary from shaly-limestone to slaty-limestone, with cm-thin intercalations of clay-rich bands. The bedding surface, marked by colour contrast and/or compositional layering, is folded into cm- to m-scale folds (figure 3a). At a few outcrops where the carbonate rocks assume the slaty character, a well-developed axial plane slaty cleavage cuts the bedding surface, and the bedding/cleavage intersection lineation parallels fold hinge lines (figure 3b and c). Fold geometry, in general, varies from isoclinal in the southwestern part to open to gentle box folds in the north-eastern part of the study area (figure 2). The poles to the bedding surface lie on a broad great circle girdle due to the non-cylindrical geometry of map scale folds (figure 3d). The mesoscopic fold hinge lines, paralleling intersection lineation, plunge at varying angles towards SE on NW-striking upright axial surfaces (figure 3e, f).

Among diversely oriented multiple fracture sets, the bedding-perpendicular fractures are the most dominant and ubiquitous. The extensional nature of these fractures is evident from the termination of fractures against lithological boundaries, lack of shear offset across the fractures, and consistent spacing between successive fractures (figure 4a, b). In general, the extension fractures strike NE and dip at sub-vertical angles (figure 4c). In this study, we focus on bedding surfaces and extension fractures.

As described later, the UAV image, combined with the field evidence, shows two distinct types of geological surfaces: the bedding surfaces and the extension fractures running at high angles to the bedding surface. By processing the UAV images, we extract orientations of the bedding surfaces and
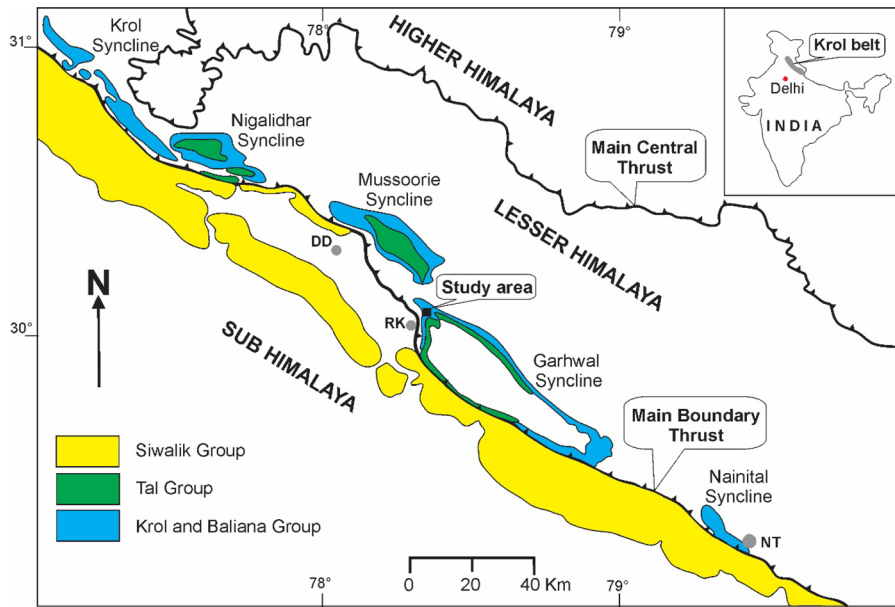
Figure 1. Krol synclines on hanging wall of the Main Boundary Thrust and the study area (after Auden 1934; Ravi Shanker Kumar *et al.* 1993; Rai *et al.* 2021; Xiao *et al.* 2022). The Shell limestone and Subathu Formations are not shown due to the limitation of scale. DD: Dehradun, RK: Rishikesh, NT: Nainital.
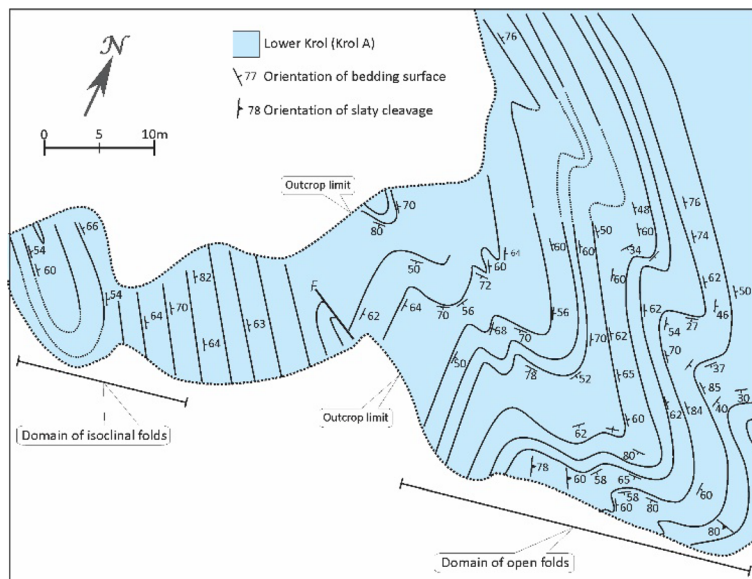

Figure 2. The study area. Map pattern of folds traced by bedding surfaces in the study area (mapped by Syed Shahid Akhtar). The folds are isoclinal in the southwestern part and open to gentle in the north-eastern part of the area.

the extension fractures and compare the results with direct field observations.

3. Material and methods

Our approach includes the UAV image acquisition and photogrammetric processing for the generation of sparse point clouds, dense point cloud, and 3-D virtual models (figure 5). Both the FACETS and the DSE software extract the modal orientations of the planar surfaces by processing the dense point cloud. Using this approach, we obtained modal orientations of bedding surfaces and extension fractures. In addition, we also extracted the orientation of a few individual bedding surfaces and fracture surfaces using the compass tool available in the cloudcompare (FACETS).

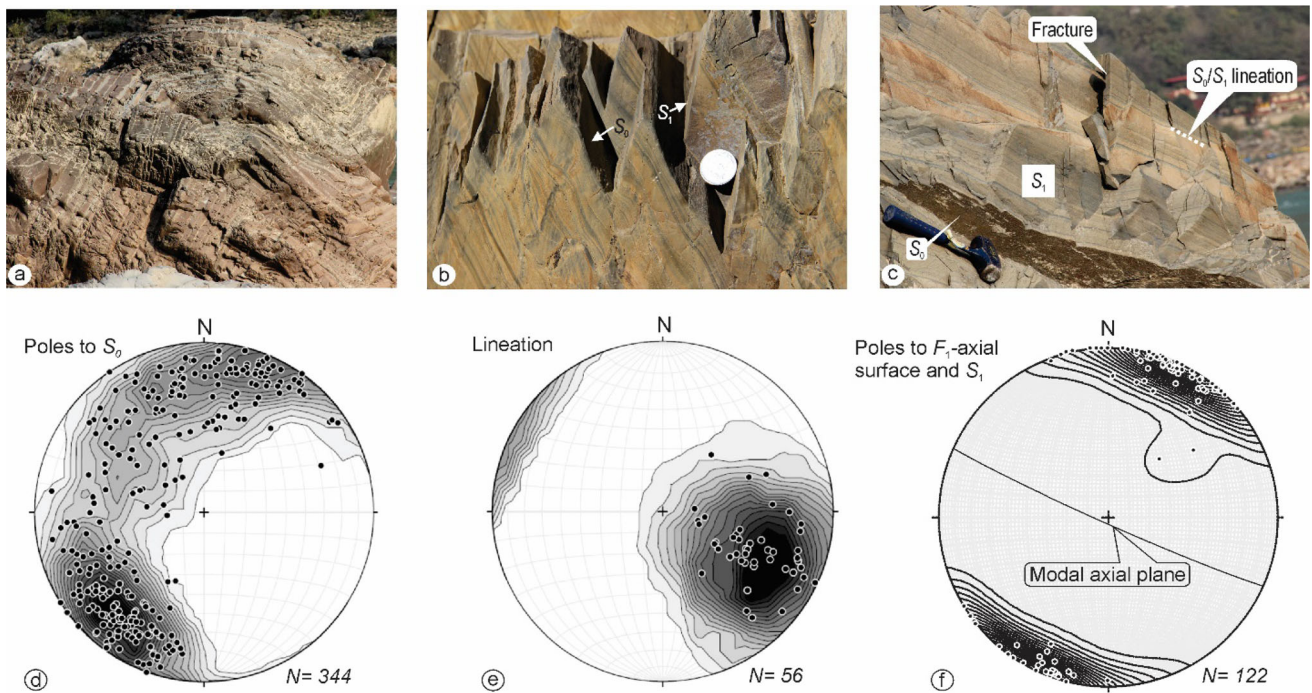A brief on the major steps of the methodology is as follows:

Figure 3. Mesoscopic structures. (**a**) Open folds in shaly-limestone interbanded with thin clay layers. Camera facing SE. (**b**) Bedding (S_0) and cleavage (S_1) in slaty-limestone. Camera facing SE. (**c**) Camera facing NW striking upright cleavage surface (S_1) in slaty-limestone. Dashed white runs parallel to S_0/S_1 intersection lineation. The bottom surface of a bedding plane is annotated as S_0. The fracture runs perpendicular to the bedding surface. (**d**) Poles to bedding surfaces (S_0). (**e**) Poles to intersection lineations and fold hinge lines. (**f**) Poles to axial surface and slaty cleavage (S_1). Great circle-Modal axial plane dips 87°/204°. Lower hemisphere equal-area projections (contours 2% per 1% area).

Figure 4. Extension fractures. (**a**) Termination of fractures at lithological boundaries. The fractures are at a high angle to the bedding surface. Camera facing NW. (**b**) Lack of shear offset in the bedding-parallel carbonate vein running across extension fractures. The carbonate vein is older than the fractures. Camera facing N. (**c**) Poles to extension fractures. Lower hemisphere equal-area projection (contours 2% per 1% area).

3.1 *UAV image acquisition*

The study area was photographed using a DJI Phantom 4 Pro (Pix4D Ltd) UAV with a 12-megapixel camera (figure 6). The parameters, such as the area of interest, overlap percentage, and flight height or desired GSD (ground sampling distance), were specified within the application. We set a moderate speed, 20 km/h, and 80% overlap for the automatic mapping by the DJI Phantom 4 Pro. The camera angle was 90° from the horizontal, and the camera face was downward. The Pix4DCapture, an Android smartphone application, was used to plan and program the auto-flight of the UAV. We scheduled 38 flights, each lasting less than 10 minutes (figure 7). A total of 611 overlapping UAV images were captured with a GSD of 0.82 cm/pixel from an elevation of 20 m. These images were automatically geotagged during the image acquisition by GPS-mounted UAV.

3.2 *Data processing and dense point cloud*

All the 611 images were processed using the structure-from-motion technique in the AGISOFT Photoscan Professional Version 1.1 software (AGISOFT PhotoScan L.L.C. 2014). Using the processed images, we obtained the sparse and dense point clouds that contain 3, 01, 931; and 56, 585, 676 points, respectively (figure 8a–c). The direct georeferencing of point clouds was enabled using the global coordinate system WGS 1984. The

entire point cloud creation took 11 hours of processing in Lenovo core i7 11th generation system. This time may vary with the processing speed of the system. The processing of dense point clouds gave the 3-D virtual model showing the ground features (figure 6).

3.3 *The DSE and the FACETS software*

The DSE is an open-source MATLAB-based software developed by the University of Alicante, Spain (Riquelme *et al.* 2014). The software searches such a set of points that correspond to a consistent planar orientation. Once the sets of points have been detected, the DSE estimates the best-fit plane using the co-planarity test (Riquelme *et al.* 2014). Finally, it gives the modal orientation of several sets of surfaces, including those representing noise, from the 3-D point clouds in a tabular form. With the help of field evidence and a virtual model, the user selects the desired surfaces from the table displaying the DSE results.

The FACETS is a plugin of cloudcompare software. It extracts a planar surface by segmenting the 3-D point clouds with a user-defined degree of co-planarity using the Kd-tree or fast marching method (Dewez *et al.* 2016). The Kd-tree method, used in this study, subdivides the 3-D point clouds into quarter cells down, in recursion, until the points contained in the cell define the best-fit
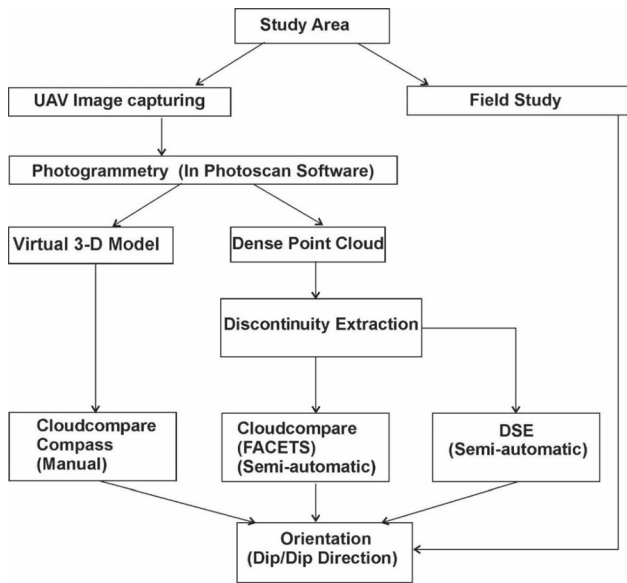

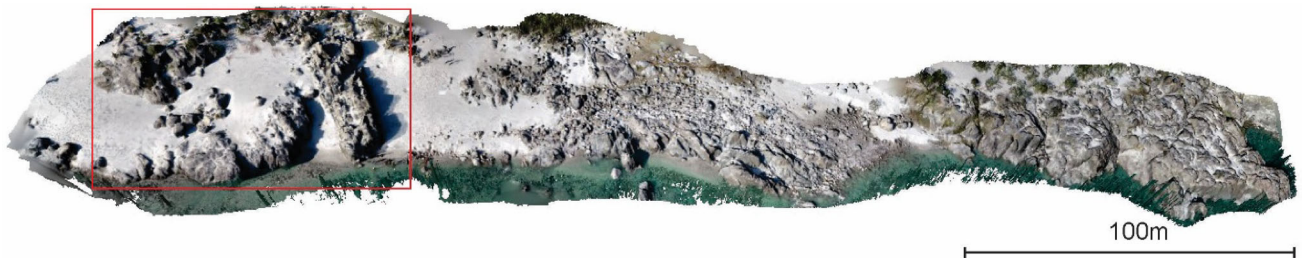Figure 5. Workflow of the methodology.

Figure 6. UAV model shows the carbonate sequence of the Krol-A Formation. The area in red rectangle is used for semi-automatic extraction of orientation of geological surfaces.
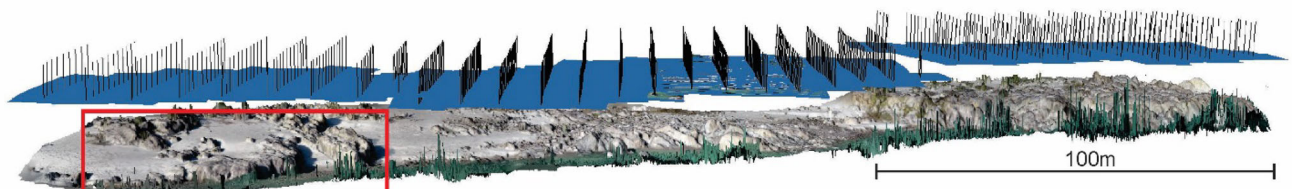

Figure 7. Camera positions on 3-D virtual outcrop model. Each black vertical line indicates the camera position and each array of black lines is a flight. Red rectangle: Area used for automatic extraction of data from software.
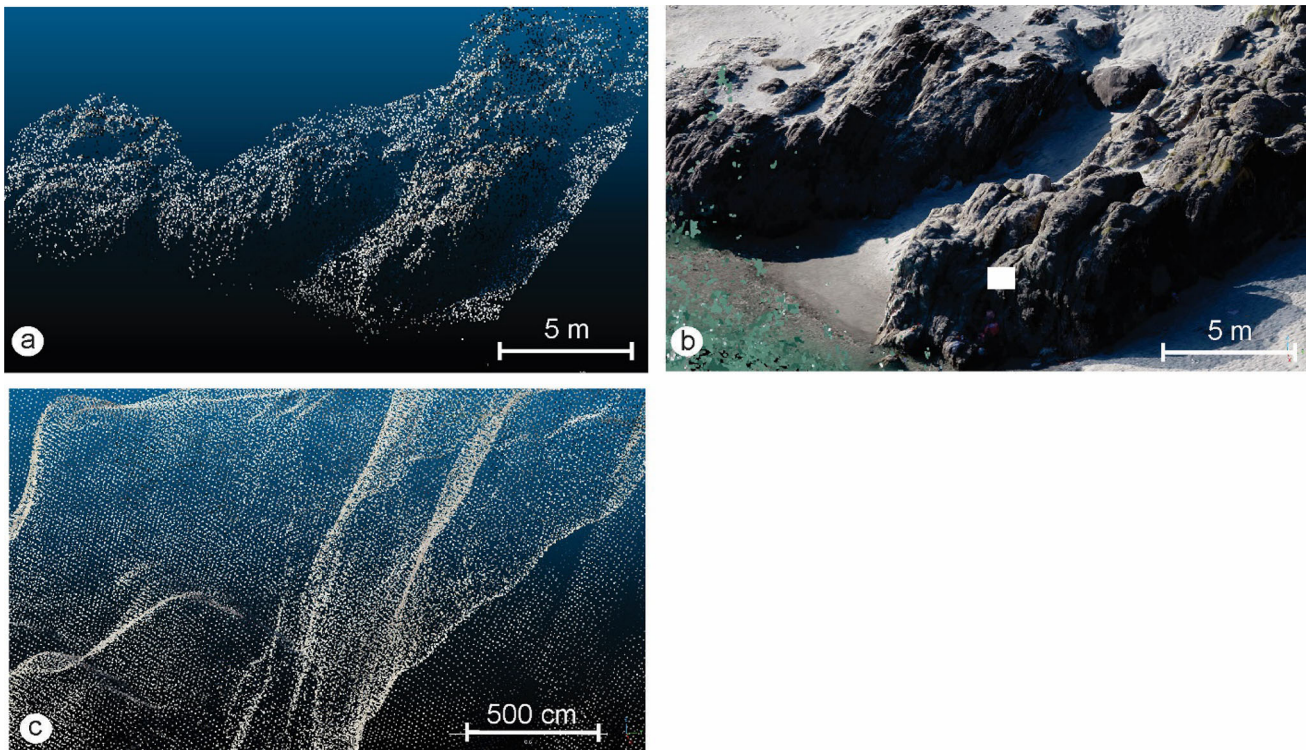
Figure 8. Point clouds for a part of the study area (red rectangle in figure 7). (**a**) Sparse point cloud. (**b**) Dense point cloud. (**c**) Points in zoomed image of area marked by white rectangle in (**b**).
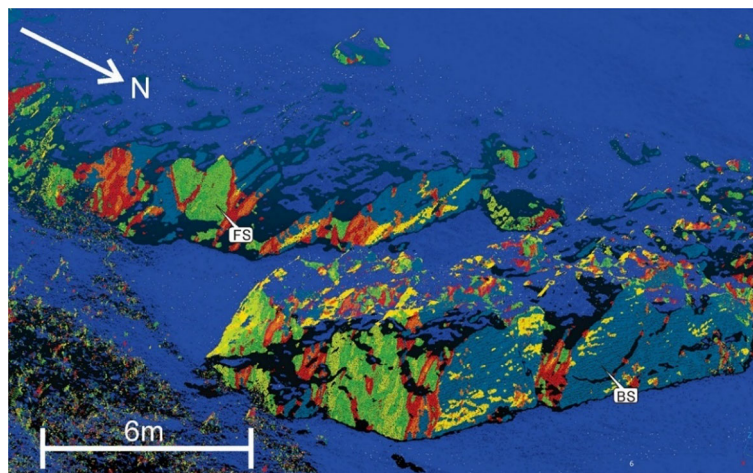

Figure 9. Result of the DSE. Each colour denotes a particular set of planes having similar orientations. Multiple colours are due to large noise. The green and the blue are the fracture surface (FS) and the bedding surface (BS), respectively.

plane. Cells containing less than six points are discarded. The output is a virtual model that contains several differently coloured domains corresponding to different sets of surfaces. A user can directly delete the domains of noise on the virtual model. The step produces an output that contains modal orientation of the desired surface only.

In practice, the output from both the DSE and the FACETS, display many sets of surfaces that are marked by different colours on virtual model (figures 9, 10). A substantial number of such surfaces are noise corresponding to the eroded or broken outcrops. For a meaningful interpretation, it is imperative to filter out the noise with the help of field observations. It is obvious that the time taken to filter the noise varies with the number of undesired surfaces in different orientations.

In addition to the above, we used Breithaupt Kassel Clar Compass, with accuracy ±1–2°, for field observations.
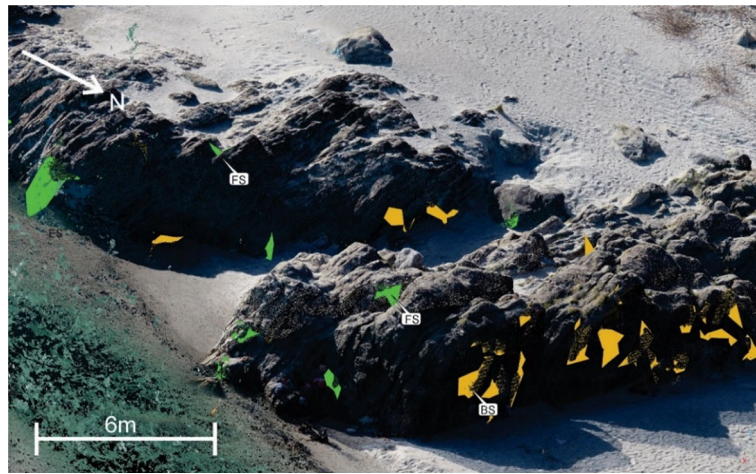
Figure 10. Result of the FACETS after filtering out the noise. Green: fracture surface, yellow: bedding surface.
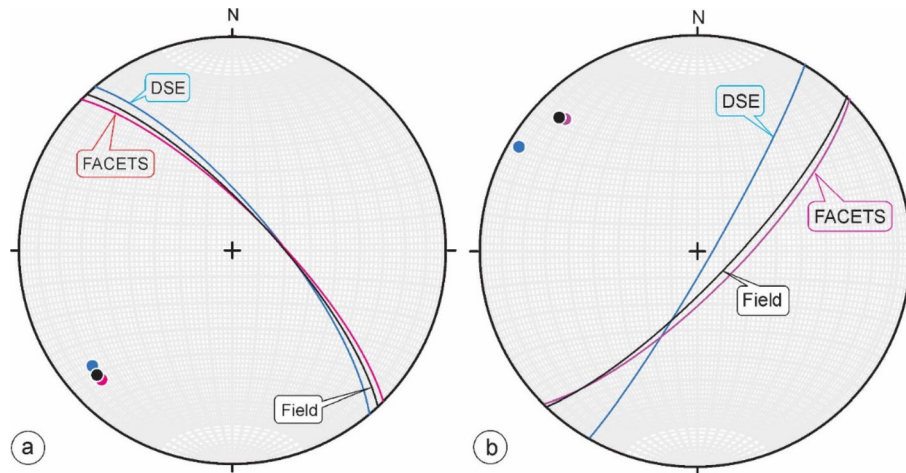

Figure 11. Comparison of modal orientations. Modes of bedding and fractures (black great circle), observed directly in field, correspond to the maxima of contoured poles. These modes are compared with modal orientations, red and blue great circles, given by DSE and FACETS software, respectively. (**a, b**). Filled coloured circles: pole to modal surface. Black: field observations, blue: DSE, and red: FACETS.

4. Errors in modal surface orientation

Both the FACETS and the DSE software gave modal orientations of all the bedding surfaces and the extension fractures in the study area. For error estimation, we compared the software-derived modal orientations with the modal orientations corresponding to the maximum of contoured stereographic plots (figures 3d, 4c, and 11a, b).

In the DSE, the absolute errors in dip angle and dip direction of bedding are of the order of 3° and 5°, respectively. In the FACETS, these errors are 2° and 0°, respectively (table 1). For extension fractures, the errors in dip angle and dip direction are 7° and 14° in the DSE and 3° and 1° in the FACETS, respectively (table 2). Our results show that the FACETS gives more accurate results than

the DSE. This inference is consistent with a recent study by Herrero *et al.* (2022). The higher accuracy of FACETS is largely due to the option for filtering out the noise.

5. Errors in individual surface orientation

For comparing the individual surface orientations, we selected such bedding and fracture surfaces that are distinct on the virtual model and also in the field. We extracted individual surface orientations by placing the virtual cloudcompare compass directly on these surfaces. The same surfaces were then spotted in the field for direct observations by Breithaupt Kassel Clar compass.

The comparison of individual surface orientations reveals that the dip angle obtained by using

Table 1. *Comparison of the modal bedding surface orientations obtained from field observations with those given by the DSE and FACETS.*

Modal orientation of bedding surface (dip angle/dip direction)

			Error	
Field observation	DSE	FACETS	DSE	FACETS
77°/045°	74°/050°	75°/045°	03°/005°	02°/000°

Table 2. *Comparison of the modal fracture orientations obtained from field observations with those given by the DSE and FACETS software.*

Modal orientation of fracture surface (dip angle/dip direction)

			Error	
Field observation	DSE	FACETS	DSE	FACETS
78°/134°	85°/120°	75°/135°	07°/014°	03°/001°

Table 3. *Comparison of the individual bedding surface orientations obtained from field observations and by using the compass tool in the Cloudcompare software. n = number of observations. Dip angle/dip direction.*

	Cloudcompare		Absolute error	
Sl. no.	compass tool	Field observation	Dip angle	Dip direction
1	81°/048°	75°/050°	06°	002°
2	76°/047°	80°/055°	04°	008°
3	72°/045°	77°/045°	05°	000°
4	55°/063°	65°/045°	10°	018°
5	80°/045°	78°/047°	2°	002°
6	74°/047°	67°/055°	7°	008°
7	78°/046°	75°/047°	3°	001°
8	81°/050°	77°/058°	4°	008°
9	77°/047°	68°/055°	9°	008°
10	68°/047°	72°/044°	4°	003°

Table 4. *Comparison of individual extension-fracture orientations obtained from field observations and by using compass tool in the Cloudcompare software. Dip angle/dip direction.*

	Cloudcompare		Absolute error	
Sl. no.	compass tool	Field observation	Dip angle	Dip direction
1	68°/295°	80°/305°	12°	010°
2	59°/291°	70°/285°	11°	006°
3	46°/321°	65°/325°	19°	004°
4	39°/322°	60°/320°	21°	002°
5	69°/331°	80°/310°	11°	021°
6	48°/312°	70°/300°	22°	012°
7	68°/303°	70°/285°	02°	018°
8	38°/328°	45°/325°	07°	003°
9	46°/325°	55°/310°	09°	015°
10	58°/310°	64°/302°	06°	008°

the compass tool in cloudcompare differs from the direct field observation by 10–20° (tables 3, 4). However, the difference in the dip direction is lower, 2–6° (tables 3, 4). A much larger difference, of the order of 23° in dip angle and 45° in dip direction, is reported by Herrero *et al.* (2022). The

dip angle obtained by direct field observations is generally steeper than that obtained by the compass tool. The reason for these variations is, as yet, unknown.

6. Discussion and conclusions

The UAV-based techniques are particularly useful for the determination of the orientations of planar surfaces in inaccessible outcrops. Steep cliffs in the gorge and canyon walls, the glacial valleys, and steep road or rail cuts are examples of such situations.

Cawood *et al.* (2017) is the only study that uses semi-automatic methods to estimate the orientations of the fold axis of the Stackpole Quay syncline, West Wales. This is achieved by intersecting the modal bedding orientations of opposite limbs of the syncline. The Stackpole Quay syncline is an ideally exposed simple syncline that folds bedding surfaces and allows UAV imaging and direct measurements. In geologically complex areas where different sets of axial plane cleavages, multiple sets of fractures, faults and erosional surfaces cut the rocks, using semi-automatic methods may be time-intensive. Similarly, in the areas of isoclinal folds with relatively small hinge zones and long limbs, the software-derived modal orientations correspond to limbs. A careful field check is, therefore, essential for correct structural interpretation. To quote Herrero *et al.* (2022), 'For the moment, 3D models will not replace field surveys because the information obtained by an experienced geologist's eye and by the rest of the senses cannot be replaced'.

One of our main objectives was to compare the results given by two alternative software, DSE and FACETS. The results show that the FACETS gives relatively more accurate results than the DSE. In our experience, the semi-automatic methods give relatively more accurate results, provided that 3-D surfaces are distinct on the virtual model. The accuracy of semi-automatic methods primarily depends on the noise level, the resolution of the photographs, and the quality of the 3-D exposure on the virtual model. In addition, the height of flight and the angle between the camera and exposed surfaces also control the accuracy. The higher the resolution and the denser the point cloud, the more accurate the results. However, a very dense point cloud may be too heavy to process by the semi-automatic software.

Author statement

Bhagirathi Panigrahi made the UAV model, processed the point clouds by DSE and FACETS, collected field data for ground check, and helped in the preparation and revision of the manuscript. D C Srivastava guided fieldwork, wrote and revised the manuscript. Sonal Tiwari acquired UAV images. Amar Agarwal conceived the problem and helped in UAV image acquisition and writing. Bitihotri Rit collected structural data in the field. Syed Shahid Akhtar mapped the study area.

References

AGISOFT PhotoScan L L C 2014 AGISOFT PhotoScan, PhotoScan User Manual Professional Edition, Version 1.1, https://www.agisoft.com/.

Akara M E M, Reeves D M and Parashar R 2020 Enhancing fracture-network characterization and discrete-fracture-network simulation with high-resolution surveys using unmanned aerial vehicles; *Hydrogeol. J.* **28** 2285–2302.

Assali P, Grussenmeyer P, Villemin T, Pollet N and Viguier F 2016 Solid images for geostructural mapping and key block modeling of rock discontinuities; *Comput. Geosci.* **89** 21–31.

Auden J B 1934 Geology of Krol Belt; *Rec. Geol. Surv. India* **64** 357–454.

Bhargava O N 1972 A reinterpretation of Krol Belt; *Him. Geol.* **2** 47–81.

Bieniawski Z 1989 *Engineering rock mass classifications: A complete manual for engineers and geologists in mining, civil, and petroleum engineering*; John Wiley & Sons, New York, 250p.

Cao T, Xiao A, Wu L and Mao L 2017 Automatic fracture detection based on Terrestrial Laser Scanning data: A new method and case study; *Comput. Geosci.* **106** 209–216.

Casini G, Hunt D W, Monsen E and Bounaim A 2016 Fracture characterization and modeling from virtual outcrops; *Am. Assoc. Pet. Geol. Bull.* **100** 41–61.

Cawood A J, Bond C E, Howell J A, Butler R W H and Totake Y 2017 LiDAR, UAV or compass-clinometer? Accuracy, coverage and the effects on structural models; *J. Struct. Geol.* **98** 67–82.

Chen J, Zhu H and Li X 2016 Automatic extraction of discontinuity orientation from rock mass surface 3D point cloud; *Comput. Geosci.* **95** 18–31.

Chen N, Kemeny J, Jiang Q and Pan Z 2017 Automatic extraction of blocks from 3D point clouds of fractured rock; *Comput. Geosci.* **109** 149–161.

Daghigh H, Tannant D, Daghigh D D, Lichti D D and Lindenbergh R 2022 A critical review of discontinuity plane extraction from 3D point cloud data of rock mass surfaces; *Comput. Geosci.* **169** 105241.

Dewez T J B, Girardeau-Montaut D, Allanic C and Rohmer J 2016 FACETS: A plugin to extract geological planes from unstructured 3D point clouds; *Int. Arch. Photogramm. Remote. Sens. Spat. Inf. Sci.*, pp. 799–804.

Ghosh T, Chattopadhyay A, Verma G, Srivastava S, Sarkar A and Bhattacharjee D 2023 Digital mapping and GIS-based spatial analyses of the Pur-Banera Group in Rajasthan, India, with special reference to the structural control on base-metal mineralization; *J. Struct. Geol.* **166** 104762.

Giordan D, Adams M S, Aicardi I, Alicandro M, Allasia P, Baldo M, De Berardinis P, Dominici D, Godone D, Hobbs P, Lechner V, Niedzielski T, Piras M, Rotilio M, Salvini R, Segor V, Sotier B and Troilo F 2020 The use of unmanned aerial vehicles (UAVs) for engineering geology applications; *Bull. Eng. Geol. Environ.* **79** 3437–3481.

Guo J, Liu S, Zhang P, Wu L, Zhou W and Yu Y 2017 Towards semi-automatic rock mass discontinuity orientation and set analysis from 3D point clouds; *Comput. Geosci.* **103** 164–172.

Herrero M J, Pérez-Fortes A P, Escavy J I, Insua-Arévalo J M, De la Horra R, López-Acevedo F and Trigos L 2022 3D model generated from UAV photogrammetry and semi-automated rock mass characterization; *Comput. Geosci.* **163**.

Hudson J 2001 *Engineering rock mechanics. Part 2: Illustrative worked examples*; MPG Books Ltd., Cornwall.

Kong D, Saroglou C, Wu F, Sha P and Li B 2021 Development and application of UAV-SfM photogrammetry for quantitative characterization of rock mass discontinuities; *Int. J. Rock Mech. Min. Sci.* 141.

Kumar G 2005 *Geology of Uttar Pradesh and Uttaranchal*; Geological Society of India, Bangalore, 383p.

Lapponi F, Casini G, Sharp I, Blendinger W, Fernández N, Romaire I and Hunt D 2011 From outcrop to 3D modelling: A case study of a dolomitized carbonate reservoir, Zagros Mountains; *Petrol. Geosci.* **17** 283–307.

Passchier C W and Exner U 2010 Digital mapping in structural geology – Examples from Namibia and Greece; *J. Geol. Soc. India* **75** 32–42.

Rai V, Shukla R, Singh A and Yadav D 2021 Geology of the Krol Belt in the Mussoorie Synform and the Garhwal Synform (along the Ganga River between Rishikesh and Devprayag), Uttarakhand, India; *J. Ind. Geol. Cong.* **12** 113–135.

Ravi Shanker Kumar G, Mathur V K and Joshi A 1993 Stratigraphy of Blaini, Infra Krol, Krol and Tal successions, Krol Belt, Lesser Himalaya; *Ind. J. Petrol. Geol.* **2** 99–136.

Riquelme A J, Abellán A, Tomás R and Jaboyedoff M 2014 A new approach for semi-automatic rock mass joints recognition from 3D point clouds; *Comput. Geosci.* **68** 38–52.

Valdiya K S 1980 *Geology of Kumaun Lesser Himalaya*; Wadia Institute of Himalayan Geology, Dehradun.

Vasuki Y, Holden E J, Kovesi P and Micklethwaite S 2014 Semi-automatic mapping of geological structures using UAV-based photogrammetric data: An image analysis approach; *Comput. Geosci.* **69** 22–32.

Viana C D, Endlein A, Campanha G A and Grohmann C H 2016 Algorithms for extraction of structural attitudes from 3D outcrop models; *Comput. Geosci.* **90** 112–122.

Vöge M, Lato M J and Diederichs M S 2013 Automated rockmass discontinuity mapping from 3-dimensional surface data; *Eng. Geol.* **164** 155–162.

Wang X, Zou L, Shen X, Ren Y and Qin Y 2017 A region-growing approach for automatic outcrop fracture extraction from a three-dimensional point cloud; *Comput. Geosci.* **99** 100–106.

Wang S, Zhang Z, Wang C, Zhu C and Ren Y 2019 Multistep rocky slope stability analysis based on unmanned aerial vehicle photogrammetry; *Environ. Earth Sci.* **78** 1–16.

Westoby M J, Brasington J, Glasser N F, Hambrey M J and Reynolds J M 2012 'Structure-from-Motion' photogrammetry: A low-cost, effective tool for geoscience applications; *Geomorphology* **179** 300–314.

Wu X, Wang F, Wang M, Zhang X, Wang Q and Zhang S 2021 A new method for automatic extraction and analysis of discontinuities based on TIN on rock mass surfaces; *Remote Sens.* **13915** 2894.

Xiao S, Jiang G, Ye Q, Ouyang Q, Banerjee D, Singh B and Hughes N 2022 Systematic paleontology, acritarch biostratigraphy, and $\delta^{13}C$ chemostratigraphy of the early Ediacaran Krol A Formation, Lesser Himalaya, northern India; *J. Paleontol.*, http://zoobank.org/5289fdb2-0e49-4b3b-880f-f5b21acab371.